Title

Direct Visualization and Manipulation of Tunable Quantum Well State in Semiconducting Nb2SiTe4

Journal

ACS Nano, 15(10)

ISSN

1936-0851

Authors

Zhang, Jing

Yang, Zhilong

Liu, Shuai

et al.

Publication Date

2021-10-26

DOI

10.1021/acsnano.1c03666

Peer reviewed

Direct Visualization and Manipulation of Tunable Quantum Well State in Semiconducting Nb_2SiTe_4

Jing Zhang[1,2‡], Zhilong Yang[3‡], Shuai Liu[1,2,4], Wei Xia[1,5], Tongshuai Zhu[3], Cheng Chen[1,6], Chengwei Wang[1,2,7], Meixiao Wang[1,5], Sung-Kwan Mo[6], Lexian Yang[8], Xufeng Kou[5,9], Yanfeng Guo[1], Haijun Zhang[3*], Zhongkai Liu[1,5*], Yulin Chen[1,5,8,10*].*

[1]School of Physical Science and Technology, ShanghaiTech University, Shanghai 201210, China

[2]University of Chinese Academy of Sciences, Beijing 100049, China

[3]National Laboratory of Solid-State Microstructures, School of Physics and Collaborative Innovation Centre of Advanced Microstructures, Nanjing University, Nanjing, 210093, China

[4]Shanghai Institute of Optics and Fine Mechanics, Chinese Academy of Sciences, Shanghai 201800, China

[5]ShanghaiTech Laboratory for Topological Physics, Shanghai 201210, China

[6]Advanced Light Source, Lawrence Berkeley National Laboratory, Berkeley, CA 94720, USA

[7]Shanghai Institute of Microsystem and Information Technology, Chinese Academy of Sciences, Shanghai 200050, China

[8]State Key Laboratory of Low Dimensional Quantum Physics, Department of Physics, Tsinghua University, Beijing 100084, China

[9]School of Information Science and Technology, ShanghaiTech University, Shanghai 201210, China

[10]Department of Physics, University of Oxford, Oxford, OX1 3PU, UK

[‡]These authors contributed equally to this work.

[*]Email address: guoyf@shanghaitech.edu.cn, zhanghj@nju.edu.cn, liuzhk@shanghaitech.edu.cn, yulin.chen@physics.ox.ac.uk

ABSTRACT: Quantum well states (QWSs) can form at the surface or interfaces of materials with confinement potential. They have broad applications in electronic and optical devices such as high mobility electron transistor, photodetector and quantum well laser. The properties of the QWSs

are usually the key factors for the performance of the devices. However, direct visualization and manipulation of such states are in general challenging. In this work, by using angle-resolved photoemission spectroscopy (ARPES) and scanning tunneling microscopy/spectroscopy (STM/STS), we directly probe the QWSs generated on the vacuum interface of a narrow band gap semiconductor Nb_2SiTe_4. Interestingly, the position and splitting of QWSs could be easily manipulated *via* potassium (K) dosage onto the sample surface. Our results suggest Nb_2SiTe_4 to be an intriguing semiconductor system to study and engineer the QWSs, which has great potential in device applications.

KEYWORDS: narrow gap semiconductor, two-dimensional material, quantum well states, band structure engineering, angle-resolved photoemission spectroscopy

Quantum well states (QWSs) can form when carriers are tightly confined to a potential well whose thickness becomes comparable to the de Broglie wavelength of the carriers, leading to energy bands with discrete energy levels (*i.e.*, sub-bands). Therefore, these states are generally found at the surface or heterostructures of materials. Such dimensionally confined electron gas can exhibit exotic quantum phenomena, for instance the high-mobility transport in metal oxide

semiconductor field effect transistors (MOSFETs),[1-3] superconductivity and magnetism in $LaAlO_3/SrTiO_3$ interface,[4-6] quantum spin Hall effect in HgTe/CdTe[7-9] and InAs/GaSb interfaces,[10, 11] and spin-momentum locking in strong topological insulators.[12-14] On the other side, QWSs are also widely used in electronic industry, including in high electron mobility transistors (HEMTs), infrared detectors, diode laser *etc.*[15-19]

The features of the QWSs, including the energy positions, splitting of the sub-bands as well as their dispersions are the key factors that determine the intriguing physical properties and the performance of the devices.[20-24] For example, the splitting of the sub-bands determines the wavelength of the lasing/absorbing photons, while the carrier concentration, effective mass and mobility strongly affect the performance of HEMTs. Over the past decades, countless efforts have been invested in generating different types QWSs devices and improving their qualities. On the other side, direct visualizing and manipulating these states are also very important to widen our understanding on the fundamental properties of this phenomenon. Angle resolved photoemission spectroscopy (ARPES) serves as a powerful tool to directly visualize the electronic structure in the momentum space. The technique has been used in the observation of the strong spin-orbit coupling QWSs formed on the Bi_2Se_3/Bi_2Te_3 surface,[25] QWSs with large

electron-phonon coupling on the surface of $SrTiO_3$ and black phosphorus,[26-28] therefore a great method for such a study.

In this work, we present the direct visualization of naturally formed QWSs on the top cleavage surface (vacuum-semiconductor interface) of a recently discovered narrow gap semiconductor Nb_2SiTe_4 and its detailed physical properties extracted (*e.g.* the energy positions, effective mass and sub-band splitting) by using the ARPES technique. In addition, we managed to manipulate the QWSs by shifting the QWSs' energy positions and tuning the sub-band splitting, through *in situ* potassium (K) dosage on the surface. The measured dispersion and evolution of the QWSs show nice agreement with our first-principles calculations. Our study reveals the existence of QWSs in a narrow gap semiconductor, and suggests a pathway to characterize and engineer the QWSs in various systems with important device applications, *e.g.* photodetectors with tunable photon energies.

RESULTS AND DISCUSSIONS

Formation of QWSs on a semiconductor surface. The schematics of the QWSs forming on the vacuum semiconductor interface were illustrated in Figure 1. Due to the breaking of translational

symmetry, an electric field builds up at the interface alongside with the bending of the conduction and valence bands. The electric fields form a surface quantum well confined to the sample surface, where the QWSs with several quantized sub-bands resides. The dispersion of such type of QWSs could be viewed as the quantized wavefunctions of electrons near E_F, as illustrated in Figure 1a(i), b(i). The typical band structure of the QWSs in semiconductors would appear dispersive along the $K_{//}$(K_x and K_y) directions, while being relatively flat along the $K_{\perp}$ (K_z) direction due to the surface confinement (Figure 1c(i)).

The surface band bending plays a critical role in the formation of the QWSs. Therefore, the QWSs could be modified by changing the surface conditions, *e.g.* by decorating the surface with K atoms (Figure 1a(ii)). The deposited K provides extra charges onto the sample surface, increasing the electric field and the extent of the band bending, thus steepens the surface potential well, as demonstrated in Figure 1b(ii). The confined QWSs are expected to evolve inside the modified potential well, with the increased splitting of the sub-bands (Figure 1c(ii)).

Crystal structure and characterizations of Nb_2SiTe_4. The formation and manipulation of this type of QWSs can be realized in Nb_2SiTe_4, a narrow gap semiconductor (gap size ~ 0.39 eV) recently discovered.[29] Nb_2SiTe_4 crystallizes in a monoclinic lattice with space group *P*121/*c*1 (No. 14)

with a layered structure shown in Figure 2a(i). Each layer is formed by the chain-like structure (Figure 2a(ii)) along the *a*-axis and the layers are bounded by van der Waals force. The surface topography on the cleaved surface of Nb_2SiTe_4 with scanning tunneling microscopy (STM) is illustrated in Figure 2b, showing nice arrangement of the topmost tellurium (Te) atoms on the (001) cleaved surface plane. The measured lattice constants obtained from the atomic resolved image are $a = 6.70$ Å, $b = 8.27$ Å, respectively. The high quality of the samples was verified by X-ray diffraction and X-ray photoemission spectroscopy (see the supporting information, Figure S1a, b).

The overall electronic band structure of Nb_2SiTe_4 is illustrated in Figure 2d (the definition of the Brillouin zone (BZ) and its projection on the (001) surface are shown in Figure 2c). From the three-dimensional plot of the photoemission spectra, as well as the dispersions along the high symmetry $\overline{Z} - \overline{\Gamma} - \overline{Z}$ (Figure 2e(i)) and $\overline{A} - \overline{\Gamma} - \overline{A}$ directions (Figure 2e(iii)), one can clearly identify an indirectly gapped semiconducting electronic structure. The valence band top is located between the $\overline{A}$ and $\overline{\Gamma}$ points while the conduction band bottom appears between the $\overline{Z}$ and $\overline{\Gamma}$ points, with the indirect gap size measured to be ~ 0.3 eV (Figure S2a). The measured

electronic structure shows nice agreement with the first-principles calculations (Figure 2e(ii), (iv)) and the previous scanning tunneling spectroscopy (STS) measurement.[34]

Interesting, several discrete bands are spotted inside the valence bands (as indicated by the arrows in Figure 2e). These discrete bands locate within the bulk band continuum and do not appear in the calculations of the bulk electronic states. Rather, these features are the manifestation of the sub-bands of the QWSs formed on the Nb_2SiTe_4 cleavage surface.

QWSs in the valence band. The QWSs could also be observed in the dI/dV curve measured by the STS (Figure 3b), where the energy intervals match well with the photoemission spectrum near $\overline{\Gamma}$ (the second derivative illustrated in Figure 3a, with the integrated energy distribution in Figure 3b), in spite of a ~200 meV global energy shift, which may come from the inhomogeneity of the sample and different probe range of STM and ARPES. Therefore, the features are excluded from the artifact caused by the photoemission matrix element or the finite K_z resolution (which would bring together the dispersion at other K_z values). In order to verify the QWSs nature of these features, we further carried out photon-energy-dependent ARPES measurement, which allows us to extract the dispersion of band structure along the $K_z(\overline{B} - \overline{\Gamma} - \overline{B})$ direction. From the extracted energy distribution curve (EDC) plot at $K_x = K_y = 0$ Å^{-1} measured at

different photon energies (Figure 3d) we find that while the intensity corresponding to the bulk bands shows clear evolution with the changing photon energies (*i.e.* along the K_z direction), the intensity of the QWSs sub-bands shows little variation, proving their two-dimensional nature (the peaks aligned by the red dotted lines).

To further understand the nature of the QWSs, we calculated the band structure of the QWSs by combining the first-principles calculation with the Poisson's equation of the one-electron surface potential *V(z)*, which is presented in detail in the method section. The calculated QWSs show multiple sub-bands with reducing energy splitting (Figure 3c), in general agrees well with the ARPES result.

Evolution of the QWSs with K dosing. As the surface potential *V(z)* plays a crucial role in the formation of the QWSs, increasing the *V(z)* by adding additional electrons through the surface dosage of K appears to be a good way to manipulate the QWSs in Nb_2SiTe_4. Detailed information about the setup of the K dosage can be found in Figure S3. With increasing K dosage, a gradual downward shift of valence and conduction bands (Figure 4a-c along the high symmetry directions $\overline{A}-\overline{\Gamma}-\overline{A}$, $\overline{Z}-\overline{\Gamma}-\overline{Z}$, and the second derivative of the later, respectively) was clearly observed, suggesting the increase of the extent of the band bending. The sub-bands

of the QWSs appear to depart from each other while shifting towards higher binding energies together (additional information can be found in Figure S2b). Such systematic evolution with the surface K dosage (increasing of the depth of the surface potential well (V_{ss})), could be repeated by our theoretical calculation (Figure 4d), which shows the same downward shift of the sub-bands and the increase of the energy intervals.

The evolution of QWSs from both the experiment and the theoretical calculation are summarized statistically in Figure 5. We plot the energy positions of the first three sub-bands as a function of the calculated K dosage level, and a similar trend can be found between the experiment (black axes) and calculation (blue axes). If we rescale the energy axis and shift the relative energy position, the two results can be well aligned. The difference here is likely due to the fact that parameters used in our calculation cannot thoroughly capture the real conditions of the material surface. Nevertheless, our simple model already quantitatively reproduced the formation and manipulation of the QWSs.

Our observation of the QWSs in Nb_2SiTe_4 provide a revenue for the investigation on this material system. As the QWSs appear in the form of flat bands along all directions near $\overline{\Gamma}$, they create large density of state at certain energy levels (0.3 to 1.2 eV from the bottom of the

conduction bands), which may lead to strong photon absorption/emission. In fact, Nb_2SiTe_4 already demonstrates strong mid-infrared response.[34] More importantly, the tunable QWSs provide the possibility to select the wavelength of the absorbed/emitted photons, therefore have great application potentials in the development of future optoelectronic devices.

We note that in addition to the K dosage in the vacuum environment, the surface potential wells which are critical to the formation of the QWSs could be created in alternative ways, such as fabricating heterostructures with materials possessing different chemical potential or applying gate voltage to the thin film of Nb_2SiTe_4. These methods could apply to the normal environment and compatible with device fabrications. For sure, different approaches for tuning the electronic structure create different physical environments for the QWSs, but the experiment carried in the UHV environment would illustrate the key physics that would hint for tuning the electronic structure in ambient environment, device design and applications.

CONCLUSIONS

In conclusion, we systematically investigated the electronic structure of the recently discovered interesting semiconductor, Nb_2SiTe_4, and confirmed the indirect band gap (~ 0.3 eV). Naturally

formed QWSs were observed on the cleavage surface of Nb_2SiTe_4, with discrete sub-bands inside the valence band. Through *in suit* surface K dosage, we are able to tune the surface potential and therefore change the position and the splitting of sub-bands of the QWSs. Our results not only reveal a fascination QWSs on the surface of a narrow band gap semiconductor, which has great application potential, but also proposes an intriguing method to probe and manipulate the QWSs, to wider our fundamental understanding of this interesting phenomenon.

METHODS

Crystal growth. Mixing powder in a mortar for 20 mins with a molar ratio of 1:2:8 of the Nb (niobium,99.95%), Si (silicon, 99.999%) and Te (tellurium, 99.99%), the completely mixed powder was placed in alumina crucible and sealed using a quartz tube at ~10^{-4} Pa. Then the tubes are healed up to 1150 ˚C in 15 h and stay for 5 h, then ramp down to 750 ˚C with a rate of 1 ˚C h^{-1} and stay for another 15 h in a high temperature well-type furnace. Extra power Si and Te will play a role of flux in reducing the melting temperature of Nb and they will be quickly removed using a centrifuge with vacuum of ~10^{-4} Pa keeping the temperature stage at 750 ˚C.

The final step is to cool down the quartz tube to room temperature in the air and then Nb_2SiTe_4 are obtained with metallic luster flakes.

STM and STS. STM used in this work is a commercial product provided by Unisoku cooperation. Nb_2SiTe_4 single crystal was cleaved in the preparation chamber and transferred *in situ* to the STM sample stage connected to a cryogenic stage kept at 77.8 K (by liquid nitrogen) for measurement under ultra-high vacuum (UHV) below 2×10^{-10} Torr. Silver islands grown on *p*-type Si (111)-7 × 7 were used to calibrate the Pt-Ir tips, which were used for both imaging and tunneling spectroscopy measurements. And the dI/dV curves are amplified by Lock-in with reference signal frequency of 997.233 HZ and amplitude of 5 mV.

ARPES. Synchrotron based ARPES measurements were performed at beam line 10.0.1 of the Advanced Light Source (ALS). The samples were cleaved *in situ* and measurements were performed under UHV below 3×10^{-11} Torr at ALS. Data were collected by a Scienta R4000 analyzer. The total energy and angle resolutions were 10 meV and 0.2˚, respectively.

Home-built helium-lamp-based ($h\nu = 21.2\ eV$) ARPES measurements were performed at ShanghaiTech University. The samples were cleaved *in situ* and measured under UHV below 4 ×

10^{-11} Mbar. Data were collected by a DA30L analyzer. The total energy and angle resolutions were 20 meV and 0.2˚, respectively. All ARPES measurements were performed at liquid nitrogen temperature.

First-principles band structure calculations. The first-principles calculations were carried out in the framework of the Perdew-Burke-Ernzerhof-type generalized gradient approximation of the density functional theory through employing the VASP package with the plane-wave pseudo-potential method.[30-32] The kinetic energy cutoff is fixed to 450 eV and the k-point mesh is taken as Γ-centered $8 \times 8 \times 8$ grid for the bulk calculations. The experimental crystal structure is taken and atomic positions are fully relaxed until the atomic force on each atom is less than 10^{-2} eV Å^{-1}. The spin-orbit coupling is included in the whole calculations. Tight-binding Hamiltonian based on Wannnier functions is constructed by projecting the Bloch states onto the Nd-4d, Te-5p orbitals.[33, 34] The surface states are calculated by the iterative Green's function method using WannierTools package.[35]

The one-electron potential $V(z)$, describing the band bending in the space-charge region as a function of depth z below a semiconductor surface, must satisfy Poisson's equation: $\frac{d^2V}{dz^2} = -$

$\frac{e}{\varepsilon_r \varepsilon_0}(-N_D + N_A - p(z) + n(z))$ with the boundary conditions: $V(z) \to 0$ as $z \to \infty$, $\frac{dV}{dz}|_{z=0} = \frac{e}{\varepsilon(0)\varepsilon_0}$ N_{ss}, where, N_D,N_A are the bulk donor/acceptor density, assumed constant throughout the semiconductor, and $p(z)$,$n(z)$ are the electron/hole density and N_{ss} is the surface state density. $n(z) = \int_0^\infty g_c(E) f_{FD} dE$, $p(z) = \int_\infty^{E_v} g_v(E)(1 - f_{FD}) dE$, $f_{FD}(E) = \frac{1}{1 + e^{\beta[E - E_F + V(z)]}}$ where $g_c(E)$, $g_v(E)$ are the density of states for the conduction and valence bands, respectively, and we get them from first-principles calculations. Here we set V_{ss} instead of N_{ss} as initial boundary conditions.

A 50-unit cell-thickness tight-binding supercell Hamiltonian, based on maximally localized Wannier functions, was constructed from first-principles calculations. In order to consider the electric-field effect, the resulting potential *V(z)* was then added to the onsite energy of the supercell tight-binding Hamiltonian.

AUTHOR INFORMATION

Corresponding Author

Yanfeng Guo – School of Physical Science and Technology, ShanghaiTech University, Shanghai 201210, China; ShanghaiTech Laboratory for Topological Physics, Shanghai 201210, China

Email: guoyf@shanghaitech.edu.cn

Haijun Zhang – National Laboratory of Solid-State Microstructures, School of Physics and Collaborative Innovation Centre of Advanced Microstructures, Nanjing University, Nanjing, 210093, China

Email: zhanghj@nju.edu.cn

Zhongkai Liu – School of Physical Science and Technology, ShanghaiTech University, Shanghai 201210, China; ShanghaiTech Laboratory for Topological Physics, Shanghai 201210, China

Email: liuzhk@shanghaitech.edu.cn

Yulin Chen – School of Physical Science and Technology, ShanghaiTech University, Shanghai 201210, China; ShanghaiTech Laboratory for Topological Physics, Shanghai 201210, China; State Key Laboratory of Low Dimensional Quantum Physics, Department of Physics, Tsinghua University, Beijing 100084, China; Department of Physics, University of Oxford, Oxford, OX1 3PU, UK

Email: yulin.chen@physics.ox.ac.uk

Author

Jing Zhang – School of Physical Science and Technology, ShanghaiTech University, Shanghai 201210, China; University of Chinese Academy of Sciences, Beijing 100049, China

Zhilong Yang – National Laboratory of Solid-State Microstructures, School of Physics and Collaborative Innovation Centre of Advanced Microstructures, Nanjing University, Nanjing, 210093, China

Shuai Liu – School of Physical Science and Technology, ShanghaiTech University, Shanghai 201210, China; University of Chinese Academy of Sciences, Beijing 100049, China; Shanghai Institute of Optics and Fine Mechanics, Chinese Academy of Sciences, Shanghai 201800, China

Wei Xia – School of Physical Science and Technology, ShanghaiTech University, Shanghai 201210, China; ShanghaiTech Laboratory for Topological Physics, Shanghai 201210, China

Tongshuai Zhu – National Laboratory of Solid-State Microstructures, School of Physics and Collaborative Innovation Centre of Advanced Microstructures, Nanjing University, Nanjing, 210093, China

Cheng Chen – School of Physical Science and Technology, ShanghaiTech University, Shanghai 201210, China; Advanced Light Source, Lawrence Berkeley National Laboratory, Berkeley, CA 94720, USA

Chengwei Wang – School of Physical Science and Technology, ShanghaiTech University, Shanghai 201210, China; University of Chinese Academy of Sciences, Beijing 100049, China; Shanghai Institute of Microsystem and Information Technology, Chinese Academy of Sciences, Shanghai 200050, China

Meixiao Wang – School of Physical Science and Technology, ShanghaiTech University, Shanghai 201210, China; ShanghaiTech Laboratory for Topological Physics, Shanghai 201210, China

Sung-Kwan Mo – Advanced Light Source, Lawrence Berkeley National Laboratory, Berkeley, CA 94720, USA

Leixian Yang – State Key Laboratory of Low Dimensional Quantum Physics, Department of Physics, Tsinghua University, Beijing 100084, China

Xufeng Kou – ShanghaiTech Laboratory for Topological Physics, Shanghai 201210, China; School of Information Science and Technology, ShanghaiTech University, Shanghai 201210, China

Author Contributions

Z.L. and Y.C. conceived the project; J.Z., C.C. and S.K.M. performed the ARPES and XPS study with the help from L.Y.; Z.Y., T.Z. and H.Z. performed the theoretical calculation; S.L. and M.W. performed the STM study; W.X. and Y.G. synthesized the crystals and performed the XRD measurement. All authors contributed to the preparation of the manuscript.

J.Z. and Z.Y. contributed equally to this work.

Notes

The authors declare no competing financial interest.

ACKNOWLEDGMENT

The authors thank H.Y., H.Z. and A.L. for helpful discussions. We acknowledge the Beamline 10.0.1 of the Advanced Light Source (ALS), beam line BL03U of Shanghai Synchrotron Radiation Facility (SSRF), China, and beam line BL13U of National Synchrotron Radiation

Laboratory (NSRL), China, for accessing and preliminary ARPES studies. The work is supported by the National Key R&D program of China (Grants No.2017YFA0305400). We thank the support from Analytical Instrumentation Center (contract no. SPST-AIC10112914), SPST, ShanghaiTech University. We acknowledge Natural Science Foundation of Jiangsu Province (No. BK20200007), the Natural Science Foundation of China (Grants No. 12074181 and No. 11834006) and the Fok Ying-Tong Education Foundation of China (Grant No. 161006).

ASSOCIATED CONTENT

The following files are available free of charge.

Supporting Information. Additional figures and data to support the results in the main text: powder X-ray diffraction aligned along the (001) crystal plane; X-ray photoelectron spectroscopy showing elements component; EDCs of ARPES at the top of valence band and the bottom of the conduct band showing an indirect band gap; EDCs of ARPES near the $\overline{\Gamma}$ point along the $\overline{Z} - \overline{\Gamma} - \overline{Z}$ direction with QWSs peaks labeled; The setup of vacuum potassium dosing and sample cleavage; The estimation of the monolayer of K dosage; Evolution of XPS spectra of K dosed Nb_2SiTe_4; The constant energy contour of Nb_2SiTe_4 at E_F with K dosage; The QWSs structure of Nb_2SiTe_4 obtained through projecting the electronic states to different unit layer. The band structure evolution with surface potential V_{ss} from two path *A-G-A* and *Z-G-Z.* (PDF)

REFERENCES

1. Seabaugh, A. C.; Zhang, Q. Low-Voltage Tunnel Transistors for Beyond CMOS Logic. *Proc IEEE.* **2010,** *98* (12), 2095-2110.

2. Ferain, I.; Colinge, C. A.; Colinge, J.-P. Multigate Transistors As the Future of Classical Metal–Oxide–Semiconductor Field-Effect Transistors. *Nature.* **2011,** *479* (7373), 310-316.

3. Liu, H.; Neal, A. T.; Zhu, Z.; Luo, Z.; Xu, X.; Tománek, D.; Ye, P. D. Phosphorene: An Unexplored 2D Semiconductor with a High Hole Mobility. *ACS Nano.* **2014,** *8* (4), 4033-4041.

4. Caviglia, A. D.; Gariglio, S.; Reyren, N.; Jaccard, D.; Schneider, T.; Gabay, M.; Thiel, S.; Hammerl, G.; Mannhart, J.; Triscone, J. M. Electric Field Control of the $LaAlO_3$/SrTiO3 Interface Ground State. *Nature.* **2008,** *456* (7222), 624-627.

5. Ohtomo, A.; Hwang, H. Y. a High-Mobility Electron Gas at the $LaAlO_3$/$SrTiO_3$ Heterointerface. *Nature.* **2004,** *427* (6973), 423-426.

6. Reyren, N.; Thiel, S.; Caviglia, A. D.; Kourkoutis, L. F.; Hammerl, G.; Richter, C.; Schneider, C. W.; Kopp, T.; Rüetschi, A. S.; Jaccard, D.; Gabay, M.; Muller, D. A.; Triscone, J. M.; Mannhart, J. Superconducting Interfaces Between Insulating Oxides. *Science.* **2007,** *317* (5842), 1196.

7. Bernevig, B. A.; Hughes, T. L.; Zhang, S. C. Quantum Spin Hall Effect and Topological Phase Transition in HgTe Quantum Wells. *Science.* **2006,** *314* (5806), 1757-1761.

8. Konig, M.; Wiedmann, S.; Brune, C.; Roth, A.; Buhmann, H.; Molenkamp, L. W.; Qi, X. L.; Zhang, S. C. Quantum Spin Hall Insulator State in HgTe Quantum Wells. *Science.* **2007,** *318* (5851), 766-770.

9. Rhiger, D. R. Chapter 6 - HgCdTe Long-Wave Infrared Detectors. In *Semiconductors and Semimetals*; Gunapala, S. D.; Rhiger, D. R.; Jagadish, C., Eds. Elsevier: 2011; Vol. 84, pp 303-331.

10. Liu, C. X.; Hughes, T. L.; Qi, X. L.; Wang, K.; Zhang, S. C. Quantum Spin Hall Effect in Inverted Type-II Semiconductors. *Phys. Rev. Lett.* **2008,** *100* (23).

11. Knez, I.; Du, R.-R.; Sullivan, G. Andreev Reflection of Helical Edge Modes in InAs/GaSb Quantum Spin Hall Insulator. *Phys. Rev. Lett.* **2012,** *109* (18), 186603.

12. Gotlieb, K.; Lin, C.-Y.; Serbyn, M.; Zhang, W.; Smallwood, C. L.; Jozwiak, C.; Eisaki, H.; Hussain, Z.; Vishwanath, A.; Lanzara, A. Revealing Hidden Spin-Momentum Locking in a High-Temperature Cuprate Superconductor. *Science.* **2018,** *362* (6420), 1271-1275.

13. He, P.; Zhang, S. S. L.; Zhu, D.; Shi, S.; Heinonen, O. G.; Vignale, G.; Yang, H. Nonlinear Planar Hall Effect. *Phys. Rev. Lett.* **2019,** *123* (1), 016801.

14. Luo, S.; He, L.; Li, M. Spin-Momentum Locked Interaction between Guided Photons and Surface Electrons in Topological Insulators. *Nat. Commun.* **2017,** *8* (1), 2141.

15. Basics of Infrared Detection. In *Quantum Well Infrared Photodetectors: Physics and Applications*; Schneider, H.; Liu, H. C., Eds. Springer Berlin Heidelberg: Berlin, Heidelberg, 2007; pp 5-12.

16. Chiang, T. C. Photoemission Studies of Quantum Well States in Thin Films. *Surf. Sci. Rep.* **2000,** *39* (7), 181-235.

17. Tournié, E.; Baranov, A. N. Chapter 5 - Mid-Infrared Semiconductor Lasers: a Review. In *Semiconductors and Semimetals*; Coleman, J. J.; Bryce, A. C.; Jagadish, C., Eds. Elsevier: 2012; Vol. 86, pp 183-226.

18. Kohler, R.; Tredicucci, A.; Beltram, F.; Beere, H. E.; Linfield, E. H.; Davies, A. G.; Ritchie, D. A.; Iotti, R. C.; Rossi, F. Terahertz Semiconductor-Heterostructure Laser. *Nature.* **2002,** *417* (6885), 156-159.

19. Arakawa, Y.; Yariv, A. Quantum Well Lasers--Gain, Spectra, Dynamics. *IEEE J. Quantum Electron.* **1986,** *22* (9), 1887-1899.

20. Ortmann, J. E.; Nookala, N.; He, Q.; Gao, L.; Lin, C.; Posadas, A. B.; Borisevich, A. Y.; Belkin, M. A.; Demkov, A. A. Quantum Confinement in Oxide Heterostructures: Room-Temperature Intersubband Absorption in $SrTiO_3/LaAlO_3$ Multiple Quantum Wells. *ACS Nano.* **2018,** *12* (8), 7682-7689.

21. Bahramy, M. S.; King, P. D.; de la Torre, A.; Chang, J.; Shi, M.; Patthey, L.; Balakrishnan, G.; Hofmann, P.; Arita, R.; Nagaosa, N.; Baumberger, F. Emergent Quantum Confinement at Topological Insulator Surfaces. *Nat. Commun.* **2012,** *3*, 1159.

22. Yoshimatsu, K.; Horiba, K.; Kumigashira, H.; Yoshida, T.; Fujimori, A.; Oshima, M. Metallic Quantum Well States in Artificial Structures of Strongly Correlated Oxide. *Science.* **2011,** *333* (6040), 319-322.

23. Hirahara, T.; Nagao, T.; Matsuda, I.; Bihlmayer, G.; Chulkov, E. V.; Koroteev, Y. M.; Echenique, P. M.; Saito, M.; Hasegawa, S. Role of Spin-Orbit Coupling and Hybridization Effects in the Electronic Structure of Ultrathin Bi Films. *Phys. Rev. Lett.* **2006,** *97* (14), 146803.

24. Alidoust, N.; Bian, G.; Xu, S.-Y.; Sankar, R.; Neupane, M.; Liu, C.; Belopolski, I.; Qu, D.-X.; Denlinger, J. D.; Chou, F.-C.; Hasan, M. Z. Observation of Monolayer Valence Band Spin-Orbit Effect and Induced Quantum Well States in MoX_2. *Nat. Commun.* **2014,** *5* (1), 4673.

25. King, P. D. C.; Hatch, R. C.; Bianchi, M.; Ovsyannikov, R.; Lupulescu, C.; Landolt, G.; Slomski, B.; Dil, J. H.; Guan, D.; Mi, J. L.; Rienks, E. D. L.; Fink, J.; Lindblad, A.; Svensson, S.; Bao, S.; Balakrishnan, G.; Iversen, B. B.; Osterwalder, J.; Eberhardt, W.; Baumberger, F.; Hofmann, P. Large Tunable Rashba Spin Splitting of a Two-Dimensional Electron Gas in Bi_2Se_3. *Phys. Rev. Lett.* **2011,** *107* (9).

26. Zhang, C.; Liu, Z.; Chen, Z.; Xie, Y.; He, R.; Tang, S.; He, J.; Li, W.; Jia, T.; Rebec, S. N.; Ma, E. Y.; Yan, H.; Hashimoto, M.; Lu, D.; Mo, S.-K.; Hikita, Y.; Moore, R. G.; Hwang, H. Y.; Lee, D.; Shen, Z. Ubiquitous Strong Electron–Phonon Coupling at the Interface of FeSe/$SrTiO_3$. *Nat. Commun.* **2017,** *8* (1), 14468.

27. Mao, N.; Wang, X.; Lin, Y.; Sumpter, B. G.; Ji, Q.; Palacios, T.; Huang, S.; Meunier, V.; Dresselhaus, M. S.; Tisdale, W. A.; Liang, L.; Ling, X.; Kong, J., Direct Oservation of Symmetry-Dependent Electron–Phonon Coupling in Black Phosphorus. *J. Am. Chem. Soc.* **2019,** *141* (48), 18994-19001.

28. Tran, S.; Yang, J.; Gillgren, N.; Espiritu, T.; Shi, Y.; Watanabe, K.; Taniguchi, T.; Moon, S.; Baek, H.; Smirnov, D.; Bockrath, M.; Chen, R.; Lau, C. N. Surface Transport and Quantum Hall Effect in Ambipolar Black Phosphorus Double Quantum Wells. *Sci. Adv.* **2017,** *3* (6), e1603179.

29. Zhao, M.; Xia, W.; Wang, Y.; Luo, M.; Tian, Z.; Guo, Y.; Hu, W.; Xue, J. Nb_2SiTe_4: a Stable Narrow-Gap Two-Dimensional Material with Ambipolar Transport and Mid-Infrared Response. *ACS Nano.* **2019,** *13* (9), 10705-10710.

30. Kresse, G.; Joubert, D. From ultrasoft Pseudopotentials to the Projector Augmented-Wave Method. *Phys. Rev. B.* **1999,** *59* (3), 1758-1775.

31. Perdew, J. P.; Burke, K.; Ernzerhof, M. Generalized Gradient Approximation Made Simple. *Phys. Rev. Lett.* **1997,** *78* (7), 1396.

32. Kresse, G.; Furthmüller, J. Efficiency of *ab-Initio* Total Energy Calculations for Metals and Semiconductors Using a Plane-Wave Basis Set. *Comput. Mater. Sci.* **1996,** *6* (1), 15-50.

33. Mostofi, A. A.; Yates, J. R.; Pizzi, G.; Lee, Y.-S.; Souza, I.; Vanderbilt, D.; Marzari, N. an Updated Version of Wannier90: a Tool for Obtaining Maximally-Localised Wannier Functions. *Comput. Phys. Commun.* **2014,** *185* (8), 2309-2310.

34. Marzari, N.; Vanderbilt, D. Maximally Localized Generalized Wannier Functions for Composite Energy Bands. *Phys. Rev. B.* **1997,** *56* (20), 12847-12865.

35. Wu, Q.; Zhang, S.; Song, H.-F.; Troyer, M.; Soluyanov, A. A. WannierTools: an Open-Source Software Package for Novel Topological Materials. *Comput. Phys. Commun.* **2018,** *224*, 405-416.

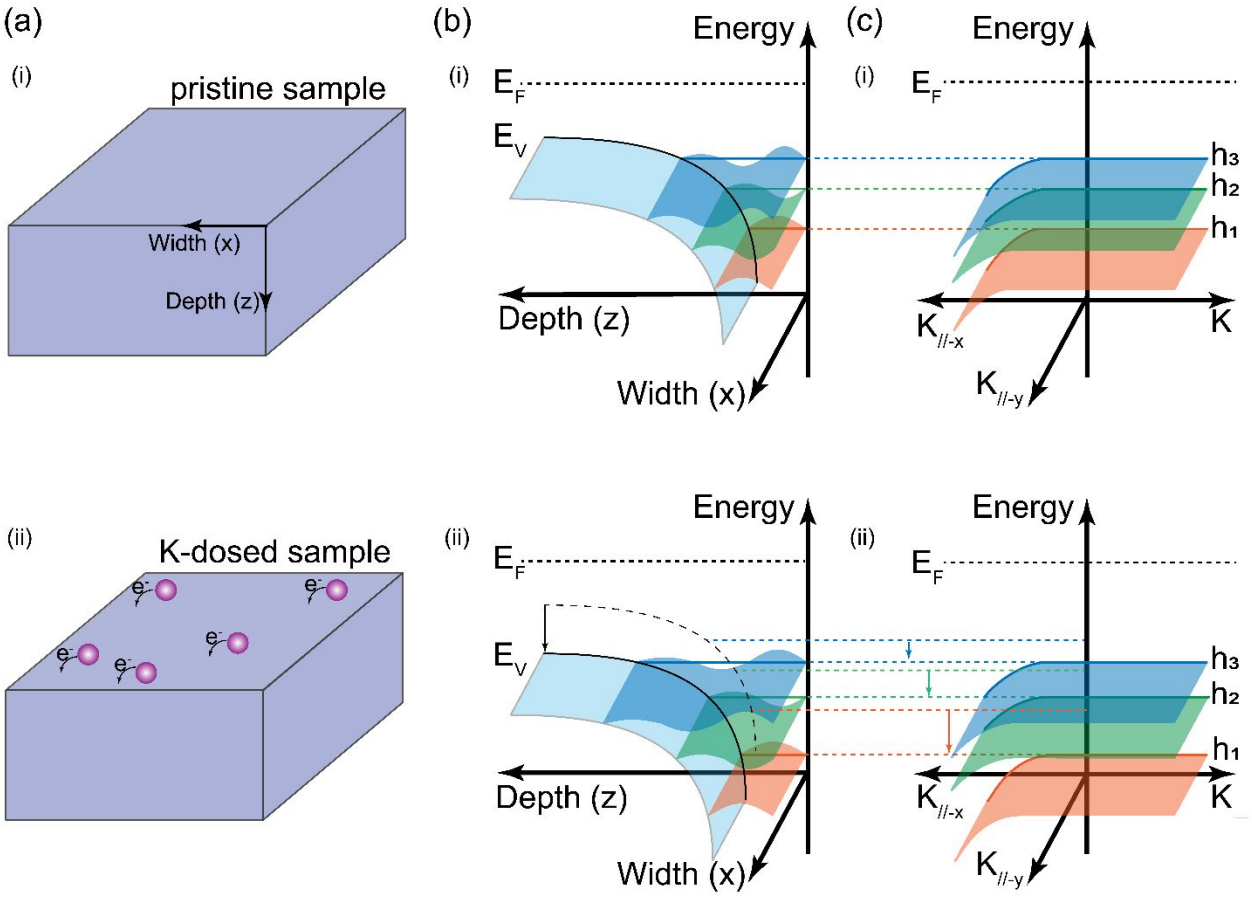

Figure 1. The formation of QWSs on a semiconductor surface. (a) Schematic of the sample surface before and after K-dosage. **(b)** Schematic of QWSs at the sample surface before and after

K-dosage. **(c)** Schematic of QWSs along parallel momentum $K_{//}$ and vertical momentum $K_{\perp}$, E_F: Fermi energy. E_v: surface potential energy.

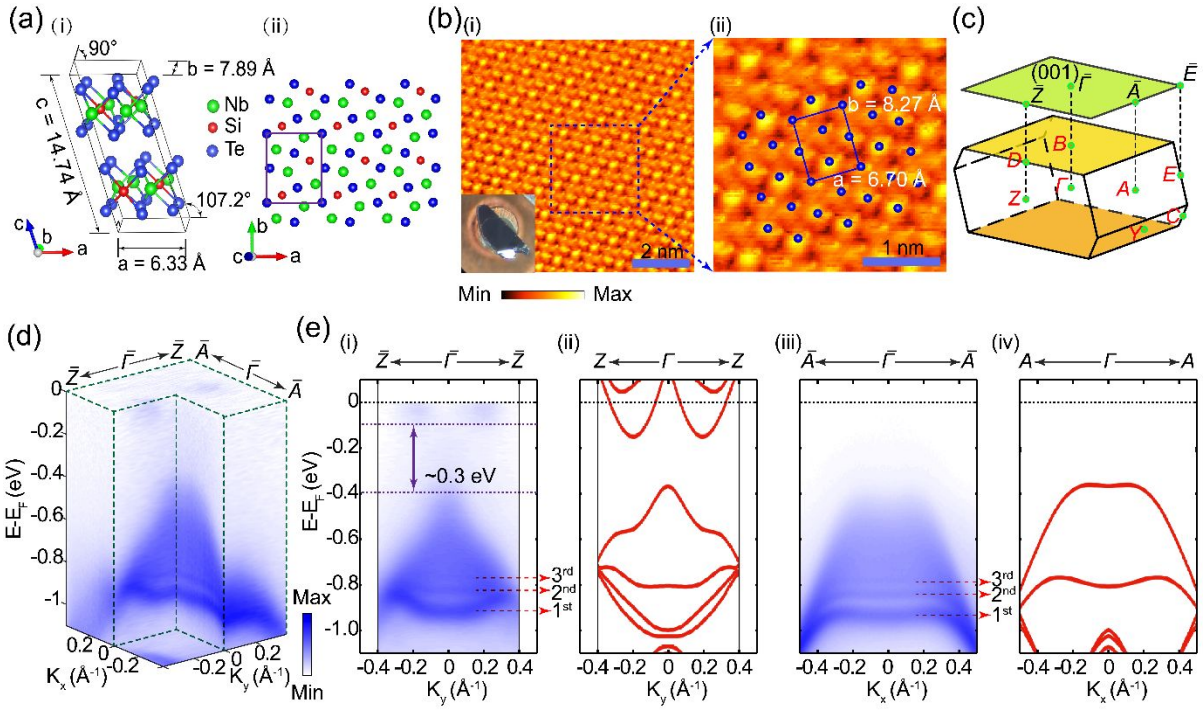

Figure 2. Crystal structure and basic characterizations of Nb_2SiTe_4. (a) Schematic of (i) the layered monoclinic crystal structure of Nb_2SiTe_4, (ii) lattice structure in the *ab* plane with one surface unit cell labelled by the blue lines. **(b)** (i) Surface topography of the (001) surface of Nb_2SiTe_4 on the 8 nm × 8 nm sample surface, with sample bias $U_s = 40$ mV and tunneling current $I_s = 500$ pA. The inset shows the picture of a high quality Nb_2SiTe_4 single crystal. (ii) Zoomed-in topography scan of an area in (i). Identified Te atom of (001) crystal plane is marked

with one surface unit cell labelled by the blue lines. **(c)** Schematic of bulk Brillouin zone and its projection to the (001) surface with high symmetry points labelled. **(d)** 3D Volume plot of the overall band structure acquired by helium-lamp-based ($h\nu = 21.2\ eV$) ARPES. **(e)** Photoemission spectra along the $\overline{Z} - \overline{\Gamma} - \overline{Z}$ (i) and $\overline{A} - \overline{\Gamma} - \overline{A}$ (iii) directions, respectively. Red arrows indicate the identified sub-bands of QWSs. An indirect band gap of ~ 0.3 eV is labelled. The results are compared with the theoretical calculations of the bulk band structure along the $Z - \Gamma - Z$ (ii) and $A - \Gamma - A$ directions (iv), respectively. Data were collected at $h\nu = 21.2\ eV$.

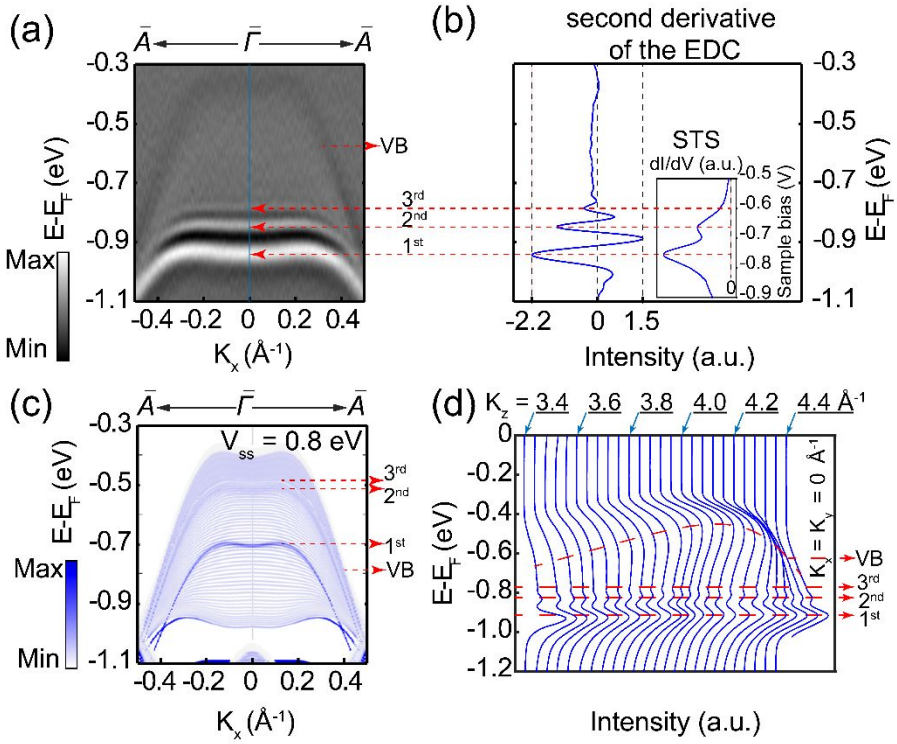

Figure 3. QWSs in the valence band. (a) Plot of the second derivative of the photoemission intensity along the $\overline{A} - \overline{\Gamma} - \overline{A}$ direction. Sub-bands of the QWSs and valence bands are labelled. Data were acquired at $h\nu = 21.2\ eV$. **(b)** Extracted second derivative of EDC from (a) near $\overline{\Gamma}$ (indicated by the blue line in (a)). The inset shows dI/dV spectrum on Nb_2SiTe_4 measured by STS at liquid nitrogen temperature with the same energy range. Red arrows indicate the identified sub-bands of QWSs. **(c)** Calculated band dispersions along the $\overline{A} - \overline{\Gamma} - \overline{A}$ direction with V_{ss} = 0.8 eV. Arrows indicate the identified QWSs and bulk valence band. **(d)** Stacked plot of EDCs at $K_x = K_y = 0$ Å^{-1} but different K_z values extracted from photon energy dependent measurement whose photon energy ranges from 37 to 69 eV. Arrows and dashed lines mark the positions of the valence band and QWSs.

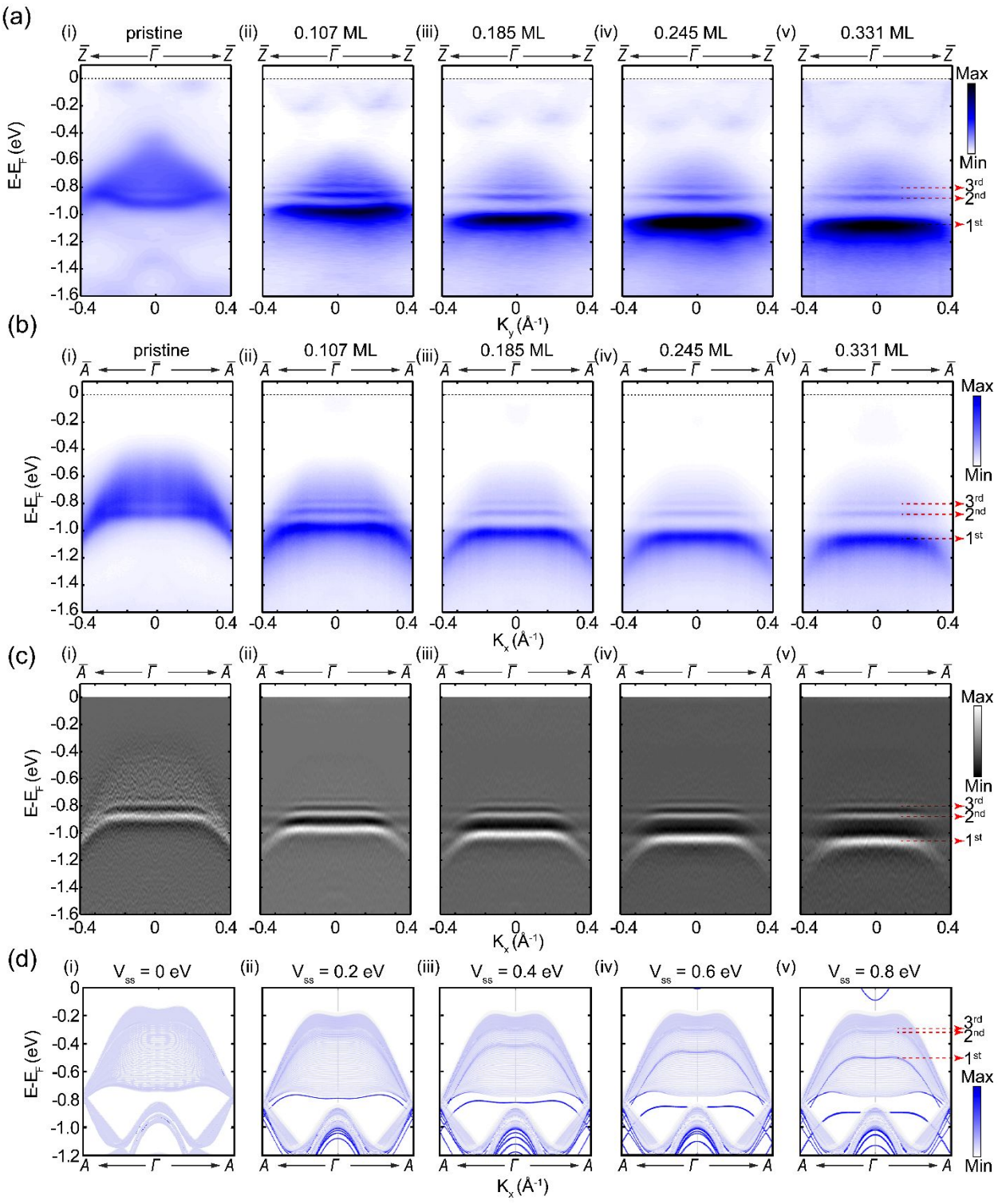
(a)
(i) pristine
(ii) 0.107 ML
(iii) 0.185 ML
(iv) 0.245 ML
(v) 0.331 ML
Z̄ Γ̄ Z̄
E-E_F (eV)
K_y (Å^-1)
Max
Min
3rd
2nd
1st
(b)
(i) pristine
(ii) 0.107 ML
(iii) 0.185 ML
(iv) 0.245 ML
(v) 0.331 ML
Ā Γ̄ Ā
E-E_F (eV)
K_x (Å^-1)
Max
Min
3rd
2nd
1st
(c)
(i)
(ii)
(iii)
(iv)
(v)
Ā Γ̄ Ā
E-E_F (eV)
K_x (Å^-1)
Max
Min
3rd
2nd
1st
(d)
(i) V_ss = 0 eV
(ii) V_ss = 0.2 eV
(iii) V_ss = 0.4 eV
(iv) V_ss = 0.6 eV
(v) V_ss = 0.8 eV
A Γ̄ A
E-E_F (eV)
K_x (Å^-1)
3rd
2nd
1st
Max
Min

Figure 4. Evolution of the QWSs with K dosing. (a) (i-v) Evolution of band dispersion along the $\overline{Z} - \overline{\Gamma} - \overline{Z}$ direction at different K dosage. **(b) (i-v)** Evolution of band dispersion along the $\overline{A} - \overline{\Gamma} - \overline{A}$ directions at different K dosage. **(c)** Second derivative analysis results of ARPES intensity in (b). **(d)** Calculated QWSs band structure at different V_{ss} values. The first three sub-bands are labeled by red arrows in (a-d). Data of (a) and (b) were acquired at $h\nu = 21.2\ eV$. The estimation of the coverage of K dosage in units of monolayer (ML) are discussed in details in the supporting information. We could also note the reduction of the bandgap in (a). The physical origin and its application are discussed in the supporting information.

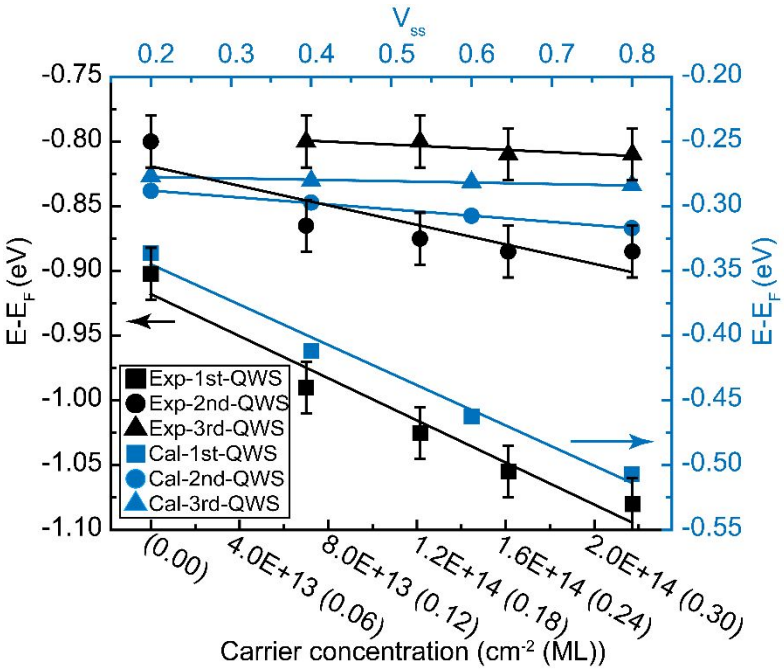

Figure 5. Summary of QWSs evolution with surface potential. The black markers are the extracted energy positions of the first three sub-bands of the QWSs from ARPES measurement

whereas the blue marks are the extracted energy positions of the first three sub-bands of the QWSs from the calculation results. The estimation of the carrier concentration from K dosage is explained in detail in the supporting information. The energies are scaled for a clear comparison of the trend of evolution.

For Table of Contents Only